Segmentation and quantitative evaluation of brain MRI data with a multi-phase three-dimensional implicit deformable model

Elsa D. Angelini[a], Ting Song[a], Brett D. Mensh[b] , Andrew Laine[a],
[a] Department of Biomedical Engineering, Columbia University, New York, NY, 10027, USA
[b] Department of Biological Psychiatry, College of Physicians and Surgeons,
Columbia University, New York, NY, 10032, USA

ABSTRACT

Segmentation of three-dimensional anatomical brain images into tissue classes has applications in both clinical and research settings. This paper presents the implementation and quantitative evaluation of a four-phase three-dimensional active contour implemented with a level set framework for automated segmentation of brain MRIs. The segmentation algorithm performs an optimal partitioning of three-dimensional data based on homogeneity measures that naturally evolves to the extraction of different tissue types in the brain. Random seed initialization was used to speed up numerical computation and avoid the need for *a priori* information. This random initialization ensures robustness of the method to variation of user expertise, biased *a priori* information and errors in input information that could be influenced by variations in image quality. Experimentation on three MRI brain data sets showed that an optimal partitioning successfully labeled regions that accurately identified white matter, gray matter and cerebrospinal fluid in the ventricles. Quantitative evaluation of the segmentation was performed with comparison to manually labeled data and computed false positive and false negative assignments of voxels for the three organs. We report high accuracy for the two comparison cases. These results demonstrate the efficiency and flexibility of this segmentation framework to perform the challenging task of automatically extracting brain tissue volume contours.

Keywords: Level set, brain MRI, segmentation, multi-phase.

1. INTRODUCTION

Segmenting three-dimensional anatomical brain images into tissue classes has applications in both clinical and research settings. As a clinical example, segmentation can provide volumetric quantification of cortical atrophy and thus aid in the diagnosis of degenerative diseases. These volumetric measurements apply to the research setting as well, where segmentation can also be used to define regions of interest for quantifying the physiological responses measured with fMRI or PET acquired on the same patients and co-registered with the MRI data.

This paper presents the implementation and quantitative evaluation of a four-phase three-dimensional active contour implemented with a level set framework for automated segmentation of brain MRIs. Level set implementation of surface propagation offers the advantage of easy initialization, computational efficiency, and the ability to capture deep sulcal folds. In recent years, several works have focused on using level set methods for MRI brain segmentation. Zeng *et al.*[1] proposed a segmentation method of the cortex from 3-D MR images using coupled level set surface propagation, assuming a constant thickness range of the cortical mantle. By evolving two embedded surfaces simultaneously, each driven by its own image-derived information while within a certain distance range from each other, an efficient segmentation of the cortical gray matter was achieved. Recently, Yang[2] *et al.* proposed a new method for 3D MR image segmentation based on the combination of joint-prior shape appearance models with a level set deformable model. This method was motivated by the observation that the shapes and gray levels variations in an image had some consistent relations. Building a MAP shape-appearance prior model provided some configurations and context information to assist the segmentation process. The model was formulated in a level set framework rather than using landmark points for parametric shape description. Goldenberg *et al.*[3] formulated their 3D MR image segmentation problem as a geometric variational problem for propagation of two coupled bounding surfaces, similar to

Medical Imaging 2004: Image Processing, edited by
J. Michael Fitzpatrick, Milan Sonka, Proceedings of SPIE Vol. 5370
(SPIE, Bellingham, WA, 2004) · 1605-7422/04/$15 · doi: 10.1117/12.535860

Zeng *et al.*[1] . The authors put forward an efficient numerical scheme for the implementation of a geodesic active surface model, where a surface evolution was performed.

In this work, we have implemented the multi-phase level set framework first proposed by Chan and Vese[4]. This framework simultaneously deforms coupled level set functions without any prior models or geometric constraints. A global partition of the image data is performed into 2^N homogenous areas for *N* level set curves, solely based on average gray values measures. Initial experiments are presented showing that MRI brain data display sufficient homogeneity to exhibit reliable segmentation performance on cortical structures using simple homogeneity measures. Quantitative evaluation of the segmentation was performed with comparison to manually labeled data and with computated false positive and false negative assignments of voxels for the three cortical structures: white matter (WM), gray matter (GM) and cerebrospinal fluid (CSF) in the ventricles.

2. METHOD

The segmentation method used in this paper is based on the Mumford-Shah functional and the implicit deformable model proposed by Chan and Vese[4].

2.1. Mumford-Shah segmentation functional

Mumford and Shah proposed a segmentation method based on a variational framework in their pioneering paper[5] in 1989. Let Ω be a bounded open set of R^N, N =2,3, and u_0 an initial image data (in 2D or 3D) define on Ω. Segmentation of the image into homogeneous objects is performed via the search for a pair of objects (u, K), where $K \subset \Omega$ is a set of discontinuities (i.e. contours), and u is a piecewise smooth approximation of u_0. The optimal definition for this pair of objects is performed via minimization of an energy functional $F(u, K)$, such that u varies smoothly within the connected components of $\Omega \setminus K$, and rapidly or discontinuously across K. The energy functional is defined in 2D as:

$$F^{MS}(u,K) = \int_{\Omega} |u - u_0|^2 dx + \mu \int_{\Omega \setminus K} |\nabla u|^2 dx + \upsilon \int_K dH^1 \qquad (1)$$

where $\mu > 0$, $\upsilon > 0$ are fixed parameters. The first term in this functional ensures that u is good approximation of u_0 , the second term ensures that u is smooth and the third term ensures that the discontinuities K have minimal length, using the one-dimensional Hausdorff measure H^1. In their seminal paper[5], the authors demonstrated the existence of a minimizer for this functional such that the edges of the image are represented in the discontinuity set K as the union of a finite set of C^1 embedded curves.

A reduced case of the above model is obtained by restricting the segmented image u to the piecewise constant functions, i.e. u = constant c_i inside each connected component Ω_i. Then the segmentation problem, called the "minimal partition problem", is solved via minimization of the following functional:

$$F_0^{MS}(u,K) = \sum_i \int_{\Omega_i} |u_0 - c_i|^2 dx + \upsilon \int_K dH^1 . \qquad (2)$$

Again, υ is a positive parameter, having a scaling role. In this case, for a fixed K, the energy in Equation (2) is minimized through computation of the variables c_i by setting c_i = mean (u_0) in Ω_i.

2.2. Active contours without edges

A new energy functional for homogeneity-based segmentation derived from the work of Mumford and Shah was proposed by Chan and Vese[6]. Let us assume that a given image, u_0 is formed by two regions of approximate

piecewise constant intensities, of distinct values u_0^i and u_0^o. Let us denote the boundary between the two regions by C_0. Given an initial curve C defined on the image, the following "fitting energy" can be minimized to segment the two regions:

$$F_1(C) + F_2(C) = \int_{inside(C)} |u_0 - c_1|^2 \, dx + \int_{outside(C)} |u_0 - c_2|^2 \, dx \, . \tag{3}$$

The parameters c_1, c_2 correspond to the mean values of the image inside and outside the curve C. As illustrated in Figure 1, the curve C_0 that corresponds to the boundary of the object minimizes this energy functional:

$$\inf_C \{F_1(C) + F_2(C)\} = 0 = F_1(C_0) + F_2(C_0) \tag{4}$$

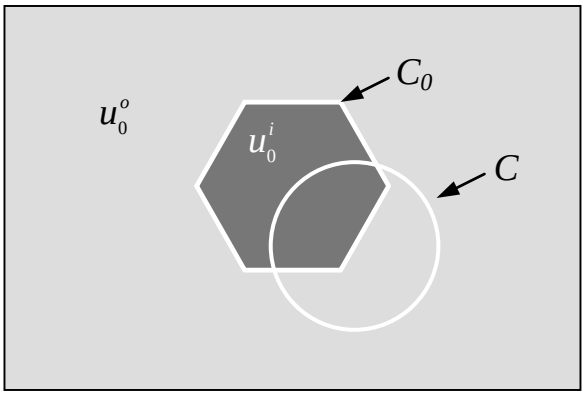

Figure 1. Segmentation of a piecewise constant image with an object and a background. Minimization of the fitting energy is achieved when the curve is on the boundary of the object.

As a special case of the Mumford-Shah functional, Chan and Vese proposed an active contour model derived from this energy functional with the addition of two regularizing terms to constrain the length of C and the area inside C:

$$F(C, c_1, c_2) = \mu(length(C)) + \upsilon(area(inside\, C)) + \lambda_1 \int_{inside(C)} |u_0 - c_1|^2 \, dx + \lambda_2 \int_{inside(C)} |u_0 - c_2|^2 \, dx \tag{5}$$

where $\mu \geq 0,\ \upsilon \geq 0,\ \lambda_1, \lambda_2 > 0$ are fixed parameters.

This energy functional can be extended to the segmentation of multiple homogeneous objects in the image by using several curves $\{C_1, C_2, ..., C_i\}$. In the case of two curves we use the following fitting energy.

$$\begin{aligned} F(C_1, C_2, c_{00}, c_{01}, c_{10}, c_{11}) = {} & \lambda_1 \int_{\substack{insideC_1 \\ insideC_2}} |u_0 - c_{11}| \, dx + \lambda_2 \int_{\substack{insideC_1 \\ outsideC_2}} |u_0 - c_{10}| \, dx + \lambda_3 \int_{\substack{outsideC_1 \\ insideC_2}} |u_0 - c_{01}| \, dx + \lambda_4 \int_{\substack{outsideC_1 \\ outsideC_2}} |u_0 - c_{00}| \, dx \\ & + \mu_1 length(C_1) + \mu_2 length(C_2) + \upsilon_1 area(insideC_1) + \upsilon_2 area(insideC_2) \end{aligned} \tag{6}$$

Minimization of this energy functional deforms simultaneously two curves and identifies four homogeneous areas defined by the intersection of the two curves as illustrated in Figure 2.

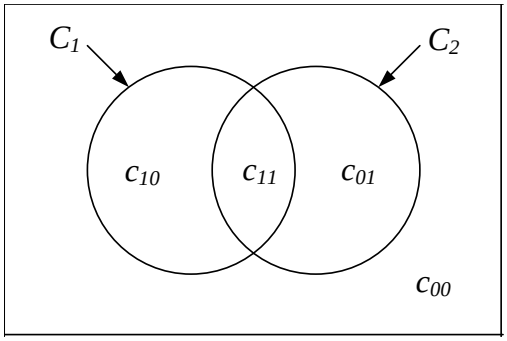

Figure 2. Partitioning of an image into four areas with two curves C_1, C_2.

2.3. Level set formulations of minimization problems

Minimization of the functional in Equations (5) and (6) is performed with a level set implementation. The level set framework, introduced by Osher and Sethian[7], provides an effective implicit representation for evolving curves and surfaces, which has found many applications, as it allows topological changes, such as merging and breaking.

A given curve C (being now the boundary of an open set $\omega \in \Omega$) is represented implicitly, as the zero level set of a scalar Lipschitz function ϕ: $\Omega \to R$ (called level set function), such that:

$$\begin{cases} \phi(x,y) < 0 & in\ \omega, \\ \phi(x,y) > 0 & in\ \Omega \setminus \omega, \\ \phi(x,y) = 0 & on\ \partial\omega. \end{cases} \tag{7}$$

Given the curve C embedded in a level set function ϕ, its associated Heaviside function H and Dirac function δ are defined respectively as:

$$H(\phi) = \begin{cases} 0, & if\ \phi \geq 0, \\ 1, & if\ \phi < 0. \end{cases} \tag{8}$$

$$\delta(\phi) = \frac{d}{d\phi} H(\phi) \tag{9}$$

Using these two functions, different components of the functional in Equation (5), parameterized with the contour curve C, can be reformulated with the level function ϕ as:

- Length of the curve C: $Length(C) = Length(\phi = 0) = \int_{\Omega} |\nabla H(\phi)|\, dx$,
- Area inside the curve C: $Area(C) = Area(\phi < 0) = \int_{\Omega} H(\phi)\, dx$,
- Average of u_0 inside the curve C: $\int_{\Omega} |u_0 - c_1|^2 H(\phi)\, dx$,
- Average of u_0 outside the curve C: $\int_{\Omega} |u_0 - c_2|^2 (1 - H(\phi))\, dx$.

The single-curve functional in Equation (5) can then be reformulated with the variable ϕ and integrals defined on the entire domain Ω:

$$F(\phi,c_1,c_2)=\lambda_1\int_{\Omega}|u_0-c_1|^2\,H(\phi)dx+\lambda_2\int_{\Omega}|u_0-c_2|^2\,(1-H(\phi))dx$$
$$+\mu\int_{\Omega}|\nabla H(\phi)|+\upsilon\int_{\Omega}H(\phi)dx \qquad (10)$$

Finally the mean values c_1 and c_2, are formulated as a function of $H(\phi)$ as:

$$c_1(\phi)=\frac{\int_{\Omega}u_0(x)H(\phi(x))dx}{\int_{\Omega}H(\phi(x))dx},\qquad c_2(\phi)=\frac{\int_{\Omega}u_0(x)(1-H(\phi(x)))dx}{\int_{\Omega}(1-H(\phi(x)))dx}. \qquad (11)$$

The Euler-Lagrange equation of this system is derived by keeping c_1 and c_2 fixed, and minimizing $F(\phi,c_1,c_2)$ with respect to ϕ as:

$$\frac{\partial\phi}{\partial t}=\delta_{\varepsilon}(\phi)\left[\mu div\left(\frac{\nabla\phi}{|\nabla\phi|}\right)-\upsilon+\lambda_1|u_0-c_1|^2-\lambda_2|u_0-c_2|^2\right]. \qquad (12)$$

In our implementation we kept the Heaviside function negative inside the contour explaining the modification of the signs of the λ_1 and λ_2 terms compared to the paper of Vese[4].

As we mentioned, this segmentation framework can be extended to the detection of multiple objects via the introduction of multiple level set functions $\{\phi_1,\phi_2,...\}$ and the computation of mean data values in areas of constant values defined via the combination of their Heaviside functions: $(H(\phi_1)\times H(\phi_2)\times...)$. In this study we implemented the segmentation functional with two level set functions generating four phases defined with mean values defined as:

$$c_{11}(\phi_1,\phi_2)=\frac{\int_{\Omega}u_0(x)H(\phi_1)H(\phi_2)dxdydz}{\int_{\Omega}H(\phi_1)H(\phi_2)dxdydz},\quad c_{10}(\phi_1,\phi_2)=\frac{\int_{\Omega}u_0(x)H(\phi_1)(1-H(\phi_2))dxdydz}{\int_{\Omega}H(\phi_1)(1-H(\phi_2))dxdydz},$$

$$c_{01}(\phi_1,\phi_2)=\frac{\int_{\Omega}u_0(x)(1-H(\phi_1))H(\phi_2)dxdydz}{\int_{\Omega}(1-H(\phi_1))H(\phi_2)dxdydz},\ c_{00}(\phi_1,\phi_2)=\frac{\int_{\Omega}u_0(x)(1-H(\phi_1))(1-H(\phi_2))dxdydz}{\int_{\Omega}(1-H(\phi_1))(1-H(\phi_2))dxdydz}. \qquad (13)$$

The Euler-Lagrange systems for the two level set functions are defined as:

$$\frac{\partial\phi_1}{\partial t}=\delta(\phi_1)\left\{\begin{array}{l}\mu div\left(\frac{\nabla\phi_1}{|\nabla\phi_1|}\right)-\upsilon+\lambda_1(u_0-c_{11})^2H(\phi_2)+\lambda_2(u_0-c_{10})^2(1-H(\phi_2))\\ -\lambda_3(u_0-c_{01})^2H(\phi_2)-\lambda_4(u_0-c_{00})^2(1-H(\phi_2))\end{array}\right\} \qquad (14)$$

$$\frac{\partial\phi_2}{\partial t}=\delta(\phi_2)\left\{\begin{array}{l}\mu div\left(\frac{\nabla\phi_2}{|\nabla\phi_2|}\right)-\upsilon+\lambda_1(u_0-c_{11})^2H(\phi_1)-\lambda_2(u_0-c_{10})^2H(\phi_1)\\ +\lambda_3(u_0-c_{01})^2(1-H(\phi_1))-\lambda_4(u_0-c_{00})^2(1-H(\phi_1))\end{array}\right\} \qquad (15)$$

We present in the next section some details on the numerical implementation for the minimization of this system of equations.

2.4. Implementation of the four-phase level set segmentation method

Segmentation is performed via iteration on the Euler-Lagrange system to deform the level set front until convergence to a stable position. The iterative scheme is therefore implemented with discretization of the system of equations as follows:

(1) Initialize system for time n=0, with $\phi^0_{1,i,j,k}$ and $\phi^0_{2,i,j,k}$ defined as the distance functions from an initial set of curves.
(2) For time n>0, while the system is unstable:
    a. Computation of the average values in the four phases c^n_{11}, c^n_{10}, c^n_{01} and c^n_{00}.
    b. Computation of the curvature terms.
    c. Computation of the density terms.
    d. Computation of $\phi^{n+1}_{1,i,j,k}$ and $\phi^{n+1}_{2,i,j,k}$.
    e. Evaluation of the stability of the system.
    f. Iteration at time n+1 if system is not stable.
(3) When system is stable:
    a. Extract the four phase binary segmented masks as the combination of inside and outside areas testing the sign of the level set functions to separate the inside and outside regions.

In our implementation, the segmentation was initialized with two level set functions defined as the distance function from two sets of initial curves. The curves were defined as 64 cylinders centered at regularly spaced seed locations across the entire data volume. The two sets of cylinders were slightly shifted from each other as illustrated in Figure 3.

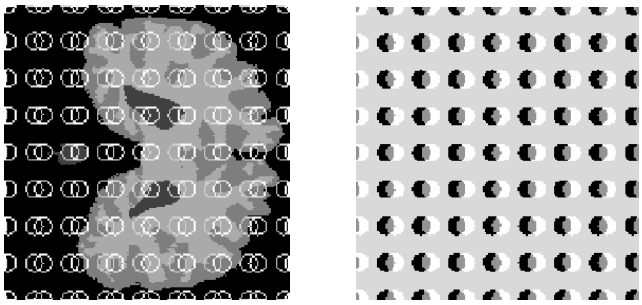

(a) **(b)**

Figure 3: Initialization of the four-phase level set segmentation method. (a) Original MRI slice with two sets of circles initialized over the entire image. (b) Corresponding partitioning of the image domain into four phases defined by the overlap of the two level set functions obtained from the circle shape.

Note that such initialization does not use any *a priori* information on the location of particular tissues or on the anatomy of the brain and does not require manual input by the user.

The level set algorithm was implemented with a semi-implicit scheme proposed by Chan and Vese[6] but extended to three dimensions. This implicit scheme provides unconditional stability for any temporal and spatial discretization parameters.

2.5. Segmentation post processing with morphological operators

Initial experiments on clinical data showed potential misclassification of tissue labels into adjacent phases at pixels located at the interface between two structures. This type of error is due to the fact that the segmentation method performs a global segmentation of the data and does not apply any constraints on the size or the shape of the tissues segmented so that misclassification of pixels might cancel each other in the homogeneity measure. To correct for these

errors we designed a simple post-processing scheme that corrected interface pixel assignments. After the level set segmentation was completed, WM, GM and CSF structures, corresponding to separate phases, were saved as binary volumes. These volumes were then used as masks applied to the original data and a Gaussian fit of the gray levels of each phase was performed. A fit of the gray-level histograms to a Gaussian distribution was performed for each structure. First, the GM mask was dilated (to correct for the under segmentation of this thin structures). Based on the normalized Gaussian fitted distribution, a threshold value was experimentally set between 0 and 1 corresponding to an interval of gray values to consider as inside the tissue of interest. Contour pixel with gray values inside this interval were kept within the GM phase, while pixels with gray values outside the interval were removed from the phase and assigned to the adjacent WM phase. This process was iterated until no new point was added in the GM phase. A similar process was then applied to the CSF phase with dilation of the binary mask. Finally, a 3-D connectivity algorithm was performed to correct for spurious isolated pixels in the three phases. This simple post-processing approach has provided very robust performance on the three clinical MRI cases segmented for this study.

3. DATA

3.1. MRI Data Sets

We applied our segmentation to one phantom and three MRI brain volumes. The three T1-weighted MRI data sets were acquired on healthy young volunteers. The MRI data sets were of size (256×256×73) with a 3mm slice thickness and 0.86mm in-plane resolution. These data sets have been previously labeled via a labor-intensive (40 hours per brain) manual method in which expert raters with extensive training in neuro-anatomy choose histogram thresholds on locally hand-drawn regions of interest. This labeled data was used as a ground truth for evaluation of the segmentation accuracy.

MRI data were pre-processed to remove all non-brain tissue by using the manually labeled data sets as binary masks. Before segmenting the data sets, we evaluated the homogeneity of the three main tissues targeted for segmentation: WM, GM and CSF. Using the labeled data as a mask, we computed the mean and variance statistics of the gray level distribution for each tissue within axial slices. These statistical measurements were performed on axial slices across the entire data volumes for the three MRI cases available for the study.

Results, illustrated in
Figure 4 showed very stable estimates of mean and variance values for each tissue type across the entire volumetric data set. Average values of the slice statistics are reported in Table 1 for the three cases.

Tissue	Mean			Standard deviation		
	Case 1	Case 2	Case 3	Case 1	Case 2	Case 3
WM	101.12	98.65	97.29	7.59	6.92	7.86
GM	73.61	71.18	69.99	9.40	10.36	8.62
CSF	36.21	40.00	38.45	13.55	15.52	13.92

Table 1. Statistics of tissue gray scale values within entire MRI volumes for the mean and standard deviation, computed for the three cases.

These results confirmed our assumption that a homogeneity-based segmentation method could be applied to these MRI data sets to extract the three main tissue types.
A Gaussian fit was performed on the histogram of the entire gray level distribution of the three brain tissues for each case. Results for our sample cases are illustrated in **Figure 4**. We observed that the three tissue types have well separated average values suggesting that the assumption of homogeneity and separability of gray scale values is valid for each patient and each tissue type. The agreement between the volume histograms and the fitted Gaussian distribution was calculated with a chi-squared test. Results for the different tissues did not show a systematic agreement between the data and the Gaussian fit, at level 0.05, except for the gray matter. Therefore, despite reasonable agreement between the data and the fitted Gaussian distribution, we need further investigation before being able to introduce additional constraints based on *a priori* Gaussian statistics to the method as proposed for example by Baillard *et al.*[8] .

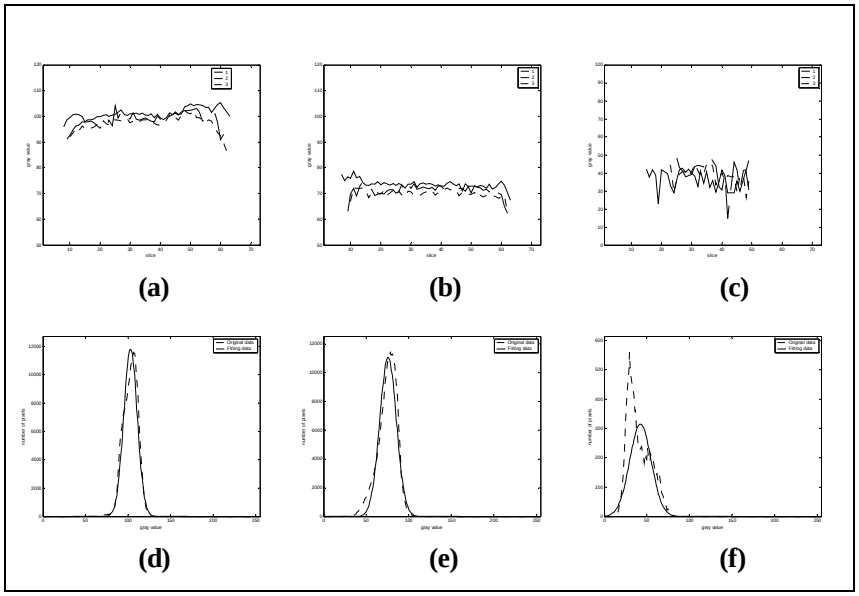

Figure 4. Statistics from (a-d) WM, (b-e) GM and (c-f) CSF gray levels. (a-c) Average values on consecutive slices within three MRI data sets represented with different line styles for the three MRI cases. (d-f) Fit of the volume histograms of case 1 to a Gaussian distribution.

We point out here that because the method only uses two level set functions, it is limited to the extraction of four homogeneous phases, corresponding to four tissue types at most. There are several other non-cortical structures in the brain such as the thalamus, including the caudate, the putamen, the pallidum, the hippocampus and the amygdala. These structures are important to extract for detection of neurological diseases such as schizophrenia or Alzheimer's disease. As shown in a recent study for manual labeling of whole brain MRI [9] data, these structures have greatly overlapping grayscale distributions. This observation explains the failure of simple thresholding methods to perform efficient extraction of these individual more subtle structures. On the other hand, as long as the histograms show reasonable compactness (with a small standard deviation), the homogeneity-based proposed method should be capable of segmenting them into separate phases. For the present study we only focused on cortical structures. Subcortical structures were therefore removed prior to segmentation using again the manually labeled data to mask them. For future applications of the method to data sets without the benefit of manually labeled data we can either use the labeling software used by clinicians to remove these structures or use an in-house "intelligent manual segmentation tool" such as the one designed by Barret *et al.*[10].

4. RESULTS

4.1. Level set segmentation set up

The level set segmentation was initialized for the phantom and three MRI cases with two sets of regularly spaced cylinders as illustrated in Figure 3. A stable behavior of the four phases was observed after 10 iterations.
Results of the segmentation on the phantom and on one clinical case are presented in Figure 5 for a single axial slice for the four phases. We observed very close visual correspondence between the volumes and the labeled data for the three structures of interest selected with the ground truth.
The results demonstrate the inherent ability of the level set framework to perform topology splitting and merging of the evolving front, enabling the identification of separate structures within a single phase (such as the first three ventricles for the CSF) that exist as different spatial objects.

4.2. Quantitative assessment of segmentation performance

Segmentation errors were measured using the recent methodology from Udupa [11] for comparison of segmentation methods. Accuracy of the object contours obtained with the proposed level set segmentation method, referred to respectively as LS and C_{LS}, is evaluated by comparing the results to our ground truth segmentation of each object, using manually labeled contours, referred to as C_{ML}. The overlap and difference between the two contours is measured via counting of true positive (*TP*), false positive (*FP*) and false negative (*FN*) pixels. These quantities are reported as volume fractions (*VF*) of the true delineated object volume C_{ML}:

- *FNVF* indicates the fraction of tissue defined in C_{ML} that was missed by the segmentation method LS.
- *FPVF* denotes the fraction of tissue defined in C_{LS} that is falsely identified by the segmentation method LS.
- *TPVF* describes the fraction of the total amount of tissue in C_{LS} which overlaps with the true object C_{ML}.

We report in the following paragraphs error measurements for segmentation on phantom and clinical MRI data sets.

4.3. Results for segmentation of MRI phantom

Segmentation results for the MRI phantom are illustrated in Figure 5 for one axial slice, displaying the four phases extracted by the level set method.

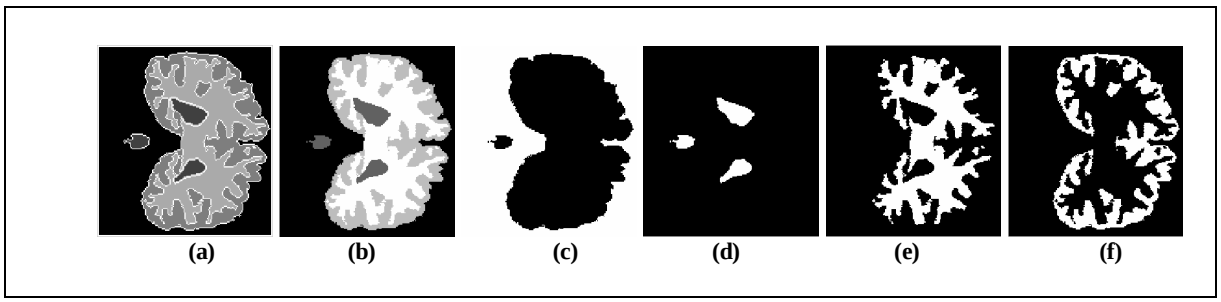

Figure 5. Phantom results of a 4 phase segmentation (a) Original image with two variable curves; (b) Synthesized image with four phases; (c) ~(f) Phase c_{11}, c_{10}, c_{01} and c_{00} respectively.

Tissue	FNVF	FPVF	TPVF
WM	0	0	100%
GM	0	0.2%	100%
CSF	15.4%	0	84.6%

Table 2: Error measurements for segmentation of MRI phantom.

This experiment showed excellent performance of the method for piecewise constant objects dividing the data space into four phases. In particular the experiment demonstrated the ability of the method to extract highly convoluted surfaces and to split a single phase into multiple objects. We also used this phantom to tune the parameters of the segmentation method set to:

$$\lambda_1 = \lambda_2 = \lambda_3 = \lambda_4 = 0.01, \upsilon = 0, \quad \mu = 4.10^{-8} \times \text{Volume\_size} / \text{Diagonal\_distance}$$

$$\Delta t = 10^4, \Delta x = \Delta y = \Delta z = 1.$$

The parameter associated with the curvature term is defined proportional to the data volume size (Volume_size) and inversely proportional to the diagonal distance of the volume data (Diagonal_distance). By doing so we consider this diagonal distance as the unitary distance of our domain of definition Ω. Setting the constant speed term υ to zero eliminates the use of a constant inflating force on the model. This type of constant force should be used with caution as it can override the homogeneity-based speed term when driving the deformable contour.

4.4. Results for segmentation of brain MRI

We present in Figure 6 a three-dimensional rendering of each segmented structure for the three MRI clinical cases segmented for this study. Visual rendering of the three cortical structures confirmed the overall high performance of the multi-phase segmentation method to extract homogenous objects that correspond to distinct anatomical tissues. The segmentation method was able to handle multiple challenges without any *a priori* information or shape constraints that include the extraction of highly-convoluted white matter surfaces, the extraction of separate ventricular structures for the CSF, and handling of different volume sizes of the three structures in a simultaneous segmentation scheme.

Error measurements for the segmentation of the three clinical cases are reported in Table 3. These results report overall clinically satisfactory (useful) performance of the proposed segmentation method.

Tissue	FNVF			FPVF			TPVF		
	Case1	Case2	Case3	Case1	Case2	Case3	Case1	Case2	Case3
WM	6.6%	4.9%	5.5%	5.9%	10.1%	5.9%	93.4%	95.1%	94.5%
GM	5.3%	6.5%	5.1%	6.5%	3.6%	5.4%	94.7%	93.5%	94.9%
CSF	24.4%	25.5%	30.9%	3.2%	1.4%	3.5%	75.6%	74.5%	69.1%

Table 3: Error measurements for segmentation of clinical MRI cases.

Significantly higher FNVF errors were observed for the CSF, corresponding to under segmentation of the ventricles, whose pixels were assigned to white matter. Very low resolution at the ventricle borders can explain in part this result. On the other hand, labeling of the MRI data for the ventricle can also bear some error as localizations of its borders is difficult even for an expert performing manual tracing. In that context, Kikinis *et a.l*[12] reported a variation in volumetric measurements of manual observers in the order of 15% for WM, GM and CSF.

We compared our error measurements to results reported by Zeng *et al.*[1] and Niessen *et al.*[13]. In Zeng *et al.*[1], the authors tested their algorithm for the segmentation of frontal lobes on seven high-resolution MRI datasets from a randomly chosen subset of young autistic and control adult subjects. They ran a coupled-surfaces level set algorithm to isolate the brain tissue and segment the cortex. The average TP and FP volume fractions for the cortical gray matter in the frontal lobe were 86.7% and 20.8%. In Niessen *et al.*[13], a 'hyperstack' segmentation method, based on multiscale pixel classification, was tested for 3D brain MRI segmentation. A supervised segmentation framework with manual post-editing was applied to a probabilistic brain phantom for estimation of segmentation error. First, a binary segmentation of the brain phantom was performed to evaluate the minimal segmentation error due to partial volume effects. The study reported a volume fraction of misclassified pixels (FP+FN) around 20% for WM, GM and CSF.

'Hyperstack' segmentation was applied with and without a probabilistic framework. Optimal (FP+FN) volume fraction errors were obtained with the probabilistic version reporting: 10% for WM, 21% for GM, and 25% for CSF.

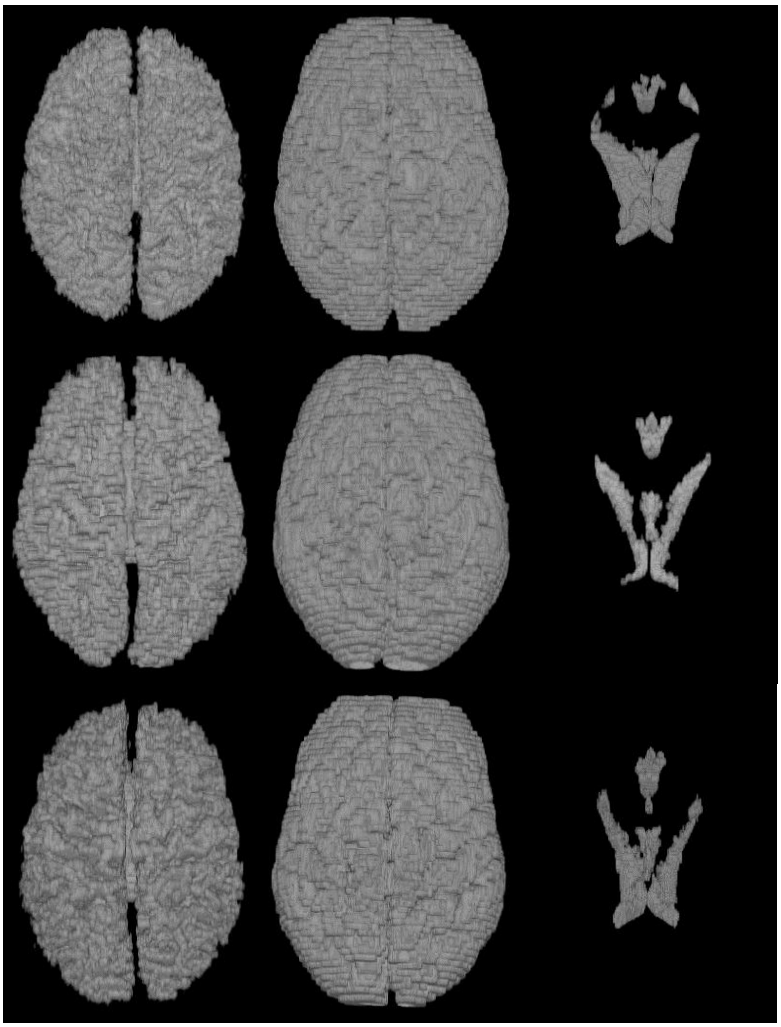

Figure 6: Three-dimensional rendering of segmented volumes for: (a) WM, (b) GM and (c) CSF of the three MRI data sets (one shown per row).

5. CONCLUSION

This paper presented a novel clinical application and quantitative evaluation of a recently introduced multiphase level-set segmentation algorithm using T1-weighted brain MRIs. The segmentation algorithm performs an optimal partitioning of a three-dimensional data set based on homogeneity measures that naturally evolves to the extraction of different tissue types in the brain. Experimentation on three MRI brain data sets showed that the optimal partitioning successfully identified regions that accurately matched WM, GM and CSF areas. This suggests that by combining the segmentation results with fiducial anatomical seed points, the method could accurately extract individual tissue types from these tissues. Random seeds for initialization was used to speed up the numerical calculation and avoid the need for *a priori* information input. This random initialization ensured robustness of the method to variation of user

expertise, biased or erroneous input information that could be influenced by variation in image quality or user expertise.

Tests on three cases demonstrated the efficiency and flexibility of this segmentation framework to perform the challenging task of automatically extracting brain tissue volume contours. Future work will include post-processing of the segmented volumes to extract individual organs as well as incorporation of available co-registered PET data to improve the segmentation performance by running the algorithm on vectorial-type data.

REFERENCES

1. X. Zeng, L. H. Staib, et al., "Segmentation and measurement of the cortex from 3-D MR images using coupled-surfaces propagation." IEEE Transactions on Medical Imaging, Vol. 18, No. 10, pp. 927-937, 1999.
2. J. Yang and J. S. Duncan, 3D Image segmentation of deformable objects with shape-appearance joint prior models, MICCAI,pp. 573-580 Montreal, Canada, 2003.
3. R. Goldenberg, R. Kimmel, et al., Cortex segmentation - a fast variational geometric approach, Variational and Level Set Methods in Computer Vision, 2001. Proceedings. IEEE Workshop on , 13 July 2001,pp. 127 - 133, 2001.
4. L. A. Vese and T. F. Chan, A multiphase level set framework for image segmentation using the Mumford and Shah model. Los Angeles, CA, USA, University of California, 2001.
5. D. Mumford and J. Shah, "Optimal approximation by piecewise smooth functions and associated variational problems." Communications on pure and applied mathematics, Vol. 42, No. pp. 577-685, 1989.
6. T. F. Chan and L. A. Vese, "Active contours without edges." IEEE Transactions on Image Processing, Vol. 10, No. 2, pp. 266 - 277, 2001.
7. S. Osher and J. A. Sethian, "Fronts propagating with curvature-dependent speed: algorithms based on Hamilton-Jacobi formulation." Journal of computational physics, Vol. 79, No. pp. 12-49, 1988.
8. C. Baillard, C. Barillot, et al., Robust Adaptive Segmentation of 3D Medical Images with Level Sets. Rennes, France, INRIA, 2000.
9. B. Fischl, D. H. Salat, et al., "Whole brain segmentation: automated labeling of neuroanatomical structures in the human brain." Neuron, Vol. 33, No. 3, pp. 341-355, 2002.
10. W. A. Barrett, L. J. Reese, et al., Intelligent segmentation tools, IEEE International Symposium on Biomedical Imaging, 2002. Proceedings,pp. Washington D.C., USA, 2002.
11. J. Udupa, V. LeBlanc, et al., A methodology for evaluating image segmentation algorithm, SPIE Conference on Medical Imaging,pp. 266-277 San Diego CA, USA, 2002.
12. R. Kikinis, M. E. Shenton, et al., "Routine quantitative analysis of brain and cerebrospinal fluid spaces with MR imaging." Journal of Magnetic Resonance Imaging, Vol. 2, No. 6, pp. 619-629, 1992.
13. W. J. Niessen, K. L. Vincken, et al., Three-dimensional MR brain segmentation, International Conference on Computer Vision,pp. 53-58 Bombay, India, 1998.